Crustal and mantle deformation inherited from obduction of the Semail ophiolite (Oman) and continental collision (Zagros)

S. Pilia[1], A. Kaviani[2], M. P. Searle[3], P. Arroucau[4], M. Y. Ali[5], and A. B. Watts[3]

[1]Department of Earth Sciences-Bullard Labs, University of Cambridge, Cambridge, UK.

[2]Institute of Geosciences, Goethe University Frankfurt, Frankfurt, Germany.

[3]Department of Earth Sciences, University of Oxford, Oxford, UK.

[4]Electricité de France, Direction Industrielle, TEGG, Aix-en-Provence, France.

[5]Department of Earth Sciences, Khalifa University of Science and Technology, Abu Dhabi, UAE.

Corresponding author: Simone Pilia (sp895@cam.ac.uk)

Key Points:

- Lithospheric deformation in the Strait of Hormuz syntaxis inferred from seismic anisotropy
- Transition from ophiolite obduction to early continental collision resulted in ~90˚ rotation of the crustal-anisotropy fast directions
- Geophysical evidence from the mantle lithosphere of NE polarity of the Late Cretaceous Oman subduction zone system

Abstract

A common deviation from typical subduction models occurs when thrust sheets of oceanic-crust and upper-mantle rocks are emplaced over more buoyant continental lithosphere. The archetypal example of ophiolite obduction is the Semail ophiolite in the United Arab Emirates (UAE)-Oman orogenic belt, formed and obducted onto the Arabian continental margin during the Late Cretaceous. The Strait of Hormuz syntaxis, the northern extent of the UAE-Oman mountains, marks the transition from ocean-continent convergence in the Gulf of Oman to continental collision along the Zagros Mountains. Based on new seismic data from a focused recording network, we infer crustal and mantle deformation in the northeastern corner of the Arabian plate (including the southern Zagros and the UAE-Oman mountains), using observations from anisotropic tomography and shear-wave splitting measurements. We recover a change of ~90˚ in the axis of fast-anisotropic orientations in the crust from the Zagros to the UAE-Oman mountain belt, consistent with the dominant strike of the orogenic belts. We also find evidence for localized fossil deformation in the lithospheric mantle underlying the UAE-Oman mountain range, possibly related to stress-induced tectonism triggered by underthrusting of the proto-Arabian continental margin beneath the overriding Semail ophiolite. These orientations, averaging 15˚ anticlockwise, provide the first geophysical verification of geological evidence that suggests a NE polarity of the Late Cretaceous Oman subduction zone system.

1 Introduction

The northeastern corner of the Arabian plate, from the Oman-UAE mountains around the Strait of Hormuz syntaxis to the Zagros Mountains in Iran, provides an excellent framework for understanding plate kinematics and geodynamics during the transition from ophiolite obduction to early continent-continent collision (Glennie et al., 1974; Searle, 2007, 2019). Indeed, the relative motion between the Arabian and Eurasian plates, resulting in convergence deformation, drives a major structural segment of the Alpine-Himalayan chain and seismic activity in the Zagros fold-and-thrust-belts (ZFTB – Figure 1). The Strait of Hormuz syntaxis in the Musandam Peninsula is the transition from the ocean-continent boundary in the Gulf of Oman to the continent-continent collision along the Zagros Mountains in Iran (Searle 1988; Searle et al., 2014).

Tectonic processes that affected the northeastern Arabian margin include continental accretion during the Precambrian-Cambrian, multiple rifting events with accompanying basin subsidence and shelf carbonate deposition from Early Permian to Early Jurassic, post-rift stable sedimentary conditions, emplacement of the Semail ophiolite in Late Cretaceous and uplift of the UAE-Oman mountains, and continental collision between the former Arabian passive margin and central Iran from Early Eocene. The Semail ophiolite in the UAE-Oman belt is the world's best example of an obducted ophiolite complex. The ophiolite formed at a fast-spreading ridge above a NE-dipping subduction zone at ca. 96.5-95 Ma (Tilton et al., 1981; Rioux et al., 2016), followed immediately by its emplacement from NE to SW onto the previously passive continental margin of Arabia. A series of allochthonous thrust sheets (Haybi and Hawasina complex thrust sheets) were emplaced structurally beneath the ophiolite to the southwest onto the Permian-Mesozoic

shelf carbonate sequence of the Arabian passive margin (Glennie et al., 1973; Searle, 2007). The resulting orogeny is the last major tectonic event that shaped the crust of the UAE and Oman. The earliest effects of the subsequent collision between Arabia and central Iran along the Zagros suture zone (~23-16 Ma) are seen in the northernmost Musandam Peninsula where Oligocene-early Miocene thrusting along the Hagab thrust records initial crustal shortening and thickening (Searle 1988, Searle et al., 2014; Ali et al., 2017). The Musandam Peninsula and its extension offshore shows a tight 90˚ bend in the strike of the orogenic belts from the southern Zagros Mountains to the UAE-Oman belt. This region has been interpreted as representing an early stage of a major orogenic-syntaxis development, analogous to the Nanga Parbat and Namche Barwa syntaxes in the Himalaya (Searle 2015a).

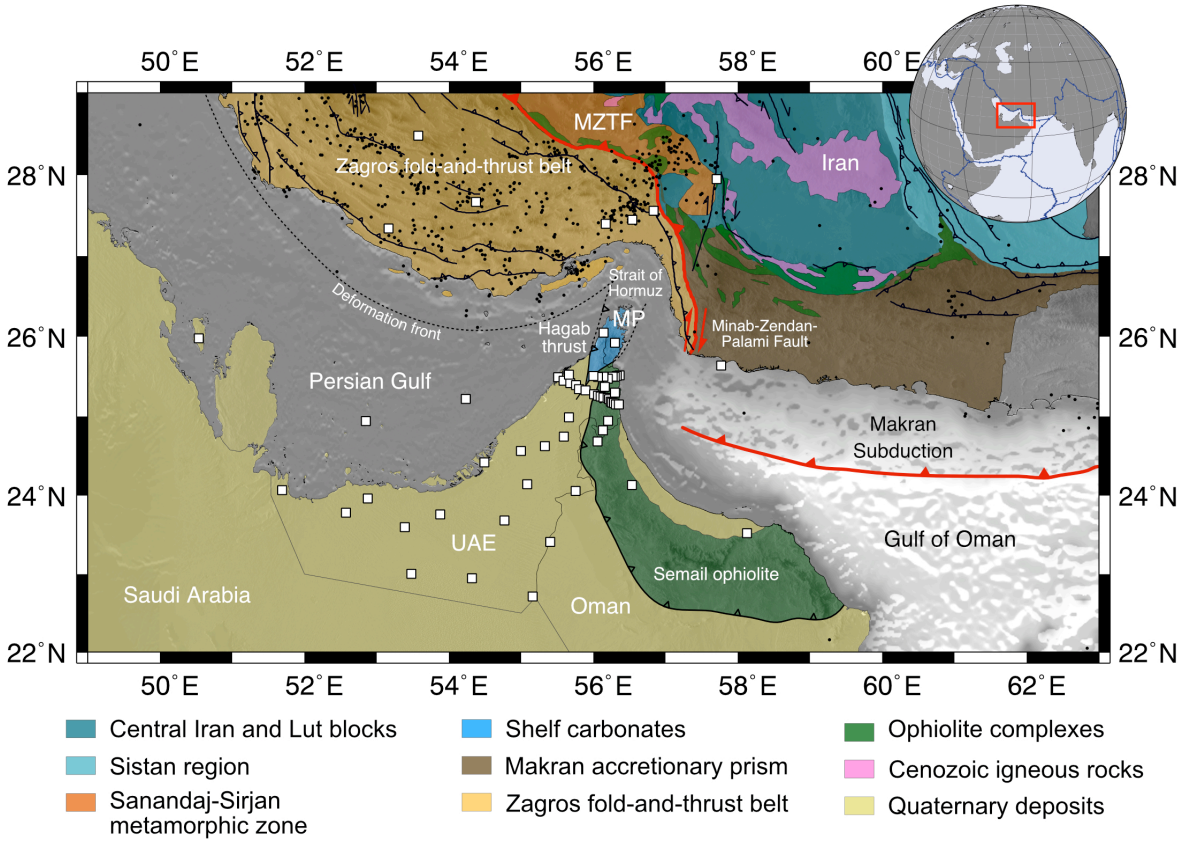

Figure 1: Simplified tectonic map of the study area as modified from the National Geoscience Database of Iran. Black lines are major faults; in the Zagros, these are generally inferred from

abrupt changes in the stratigraphic level within the Mesozoic sedimentary section. Red line is the suture boundary (MZTF: Main Zagros Thrust Fault) between the Arabian platform and central Iran. Black dots are earthquakes from the ISC catalogue. White squares are seismic stations. Background map represents shaded relief. The inset in the upper right corner shows the location of the study area. MP: Musandam Peninsula.

Previous tomographic models of the region have been coarse (e.g., Priestley et al., 2012) and, even if they have been able to illuminate relatively smaller structure, typically assume isotropic variations of the seismic wavefield (e.g., Pilia et al., 2020a; Pilia et al., 2020b), hence observational constraints on crustal and mantle deformation in the form of anisotropy are not retrieved. This has prevented previous studies from making inferences on how the lithosphere has been deformed due to complex processes such as obduction of the Semail ophiolite (and preceding subduction) and indentation of the Musandam Peninsula. A number of mechanisms are responsible for the directional dependence of seismic wave-speed but regular patterns of tectonic fabric, stress-aligned microcracks and preferred mineral alignment are generally invoked in anisotropic lithospheric studies (Babuska & Cara, 1991; Crampin, 1994). For instance, areas subject to major deformation events (e.g., orogenic belts, extensional domains) tend to inherit an anisotropic signature that is congruent with the strike of regional tectonic structures.

Coupled with a number of seismic stations in Iran, continuous seismic data recorded from a new network in the UAE represent a unique opportunity to examine and relate patterns of crustal and mantle anisotropy to dynamics in a region of convergence of orogenic belts. Here we constrain anisotropy in the crust using ambient seismic noise recordings, and account for the apparent azimuthal dependence of measured Rayleigh-wave phase velocities to test whether orogenic processes have left an imprint in the Strait of Hormuz syntaxis. In order to constrain the strength (delay time) and orientation (fast axis) of anisotropy in the underlaying mantle, we calculate the differential arrival time between orthogonal components of core seismic phases

from teleseismic earthquakes. We then reconcile both the recovered isotropic velocities and anisotropic orientations to different deformational events that have controlled the structural styles in the lithosphere beneath the seismic network. In particular, while surface geological evidence suggests that obduction of the Semail ophiolite occurred from NE to SW onto the proto-Arabian continental margin, thus far geophysical methods have not been able to image underthrusting of the continental lithosphere beneath the ophiolite sequence. However, if such underthrusting is present, it would be expected to manifest as a possible perturbation of the mantle flow, or as a "frozen-in" deformation in the tectonic fabric. It is the signature of this tectonic process that we hope to reveal from the anisotropy pattern in the upper mantle beneath the UAE-Oman range.

2 Data analysis

2.1 Anisotropic phase-velocity maps

Broadband continuous seismic records used in this study are sourced from 68 seismic stations operating in the region (Figures 1 and S1). Recording periods used in this study are generally 2.5 years, from June 2014 to December 2016 (Pilia et al., 2020a). Empirical Green's Functions (EGFs) and phase velocities are taken from Pilia et al. (2020a); the following is a short summary of the processing carried out to obtain phase velocities from the raw, continuous ambient-noise records. In order to extract the EGFs from the vertical component between all simultaneously recording stations, we employ a scheme similar to that described in Pilia et al. (2016). After removal of anomalously large amplitude events, cross-correlations are computed for all station pairs by cross-correlating the vertical component of 1 hour segments, filtered in the

range 0.03 and 2.0 Hz. We used a robust phase-weighted stacking procedure (Schimmel et al., 2011; Ventosa et al., 2017) for stacks of daily cross-correlations. Figure 2 shows the symmetric component of the cross-correlations associated with a number of stations. The application of the phase-weighted stacking algorithm of Ventosa et al. (2017) strongly reduced the incoherent noise and made vast improvements in the quality of the cross-correlograms (see Figure S2), which ultimately made the dispersion analysis much more reliable and self-consistent. It is important to note that, although earthquakes do deteriorate the quality of cross-correlations, the phase-weighted stacking is insensitive to large amplitude events (Schimmel et al., 2011). Phase-velocity dispersion measurements of the Rayleigh wave, generated in Pilia et al. (2020a), were calculated from the nearly 1500 EGFs for periods ranging from 2 to 40 seconds (although we only adopt periods from 5 to 25 for subsequent tomographic analysis). To this end, we used a semi-automated, modified version of the image transformation technique developed by Yao et al. (2006), in which the method and its application are fully illustrated (see also Pilia et al., 2016, 2020a for more details). In the first step we construct a period-time image by applying a series of narrow band-pass filters to the symmetric EGFs in the periods of interest. The width of the filters can be changed by the user and is defined as $(Period + (Value * Period))^{-1}$ and $(Period - (Value * Period))^{-1}$ for the lower and upper bound, respectively. "Value" is a real number input from the user, and we find that 0.35 gives robust results. Each filtered time series is subsequently transformed into a phase velocity-period image. The method then requires an average dispersion curve, coincident with the fundamental mode, to be defined by the user through mapping the points of all phase velocity-period images whose amplitude is greater than 0.9 times the maximum amplitude. Final Rayleigh wave path-averaged phase velocities are automatically picked for each period within the average velocity curve previously calculated, along with

155 respective uncertainties estimated as $(C_{up}(T) - C_{down}(T))/2$, with C_{up} and C_{down} corresponding to
156 the velocities at the first zero amplitude crossing prior and following the picked amplitude
157 maximum, respectively (Figure 2). Picking starts from the highest period and moves towards
158 lower periods with gradient constraints imposed to avoid discontinuous dispersion curves or
159 large, unlikely jumps in the picking. All picked phase velocity curves were visually checked and
160 modified in case the wrong average curve was used to pick the fundamental mode. Finally, we
161 only retain Rayleigh-wave phase-velocity measurements in the range of two standard deviations
162 from the mean velocity of a particular period (Figure S3).

163 In order to characterise the effects of azimuthal variations of the interstation-averaged
164 phase velocities, we invert them and map the isotropic and anisotropic wavefield components
165 over a period range of 5-25 s. The azimuthal dependence of local Rayleigh phase speed C in the
166 presence of a weak anisotropic medium can be expressed via the following relation (Smith and
167 Dahlen, 1973):

168

169 $$C(T)=C_0(T) + A_1(T)\cos(2\theta) + A_2(T)\sin(2\theta) + A_3(T)\cos(4\theta) + A_4(T)\sin(4\theta)$$

170

171 where $C_0(T)$ is the isotropic term at period T, θ is the ray propagation azimuth and A_1, A_2, A_3, and
172 A_4 are azimuthal anisotropic coefficients. The terms 2θ and 4θ exhibit a periodicity of π and $\pi/2$,
173 respectively, and account for the azimuthal variations. However, Montagner and Nataf (2016)
174 have demonstrated that 4θ coefficients normally provide very little contribution to the azimuthal
175 variability of Rayleigh wave phase velocities, hence are often ignored (Fry et al., 2010; Bao et
176 al., 2016; Rawlinson et al. 2014; Pilia et al., 2016). Therefore, what we need to compute at any
177 grid point of our model is a set of three unknowns, specifically $C_0(T)$, $A_1(T)$ and $A_2(T)$. We use

the inversion scheme of Debayle and Sambridge (2004), which is based on the continuous parameterisation algorithm of Montagner (1986), in that it uses *a priori* information on the model but improves efficiency by incorporating geometrical constraints. Smoothing regularisation is imposed through application of an *a priori* spatial correlation filter among points separated by a L_{corr} distance, while an *a priori* model standard deviation σ controls the amplitude of anomalies, thus acting as a damping constraint on the final solution.

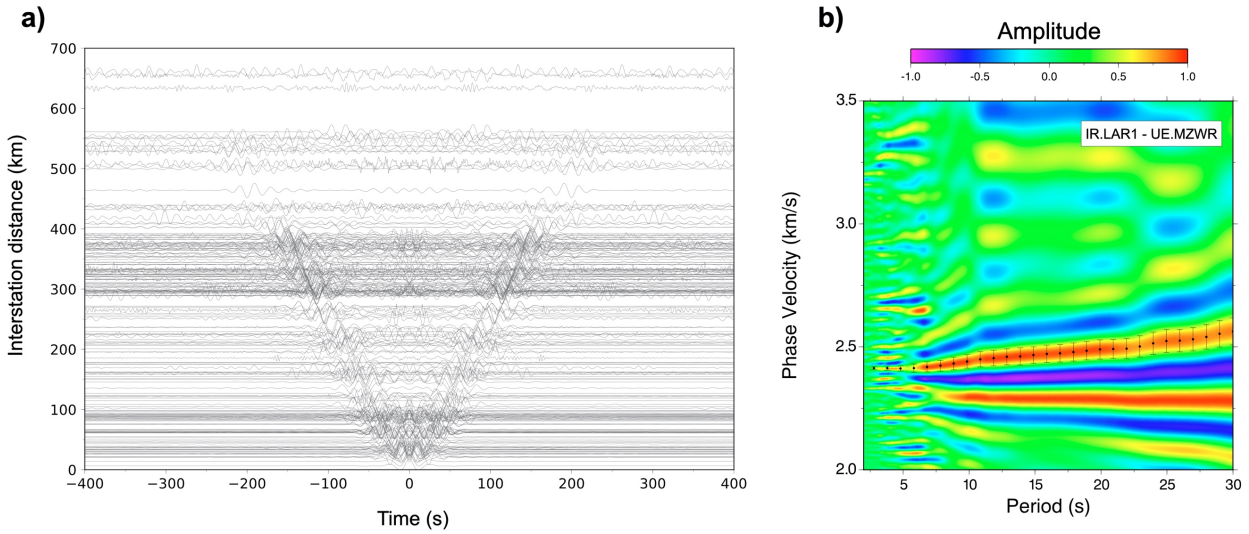

Figure 2: a) Record sections showing the emergent Rayleigh wave energy for all the possible long-term cross-correlation combinations associated with stations UE.UMZA, XX.STN25, UE.GHWR, AE.SHM (see Figure S1 for locations) and all other possible station pairs. Note that the positive and negative correlation lags have been averaged and phase-velocity dispersion measurements performed on the symmetric component. b) Example of picking of the fundamental mode for a phase dispersion curve identified from the filtered cross-correlation between station IR.LAR1 (Iran) and UE.MZWR (southwest UAE). Picked phase velocities, with relative uncertainties, are represented by black dots. Top-right inset indicates station names (see Figure S1 for location).

2.2 XKS-phase splitting

196 By entering into an anisotropic medium, a seismic shear wave splits into two quasi-shear
197 wave components with orthogonal polarization that then travel with different speeds through the
198 anisotropic medium. The heading component is polarized parallel to the fast symmetry axis of
199 anisotropy. By arriving at a seismic station, the delay (split) time between the two components is
200 an integral effect of the strength of anisotropy and the length travelled through the anisotropic
201 medium. In a shear-wave splitting (SWS) analysis, the polarization of the fast component and
202 the split time are measured and taken as a proxy for the symmetry axis and strength of the
203 underlying anisotropic medium, respectively.

204 We use records of core-refracted shear phases (SKS, PKS and SKKS, called hereinafter
205 XKS) from a total of 462 teleseismic events in the epicentral distance range 88˚-142˚ with
206 magnitude larger than 5.7 (Figure 3). In an SWS analysis for probing mantle anisotropy, the
207 aforementioned seismic phases have two main advantages over direct S-waves: 1) by converting
208 to a P-wave through the outer core, any source-side effect of anisotropy on these phases is
209 removed and therefore only receiver-side effects are retained in the split waveforms; 2) in a P-to-
210 S conversion at the core-mantle boundary, the generated Sv wave has a known polarization
211 (along the great circle connecting the source and receiver), hence the initial polarization of the
212 XKS phases is easy to estimate. The knowledge of the initial polarization is the first step of any
213 SWS analysis.

214 In a SWS analysis, the XKS waveforms at each station can be either individually or
215 jointly processed. We exploit the SplitRacer code of Reiss and Rümpker (2017) to jointly
216 analyze the XKS waveforms available from each station. The parameters of a one-layer
217 anisotropy model beneath each station are searched in order to minimize the total energy of all T-
218 components of XKS seismograms at the station. In addition, individual splitting parameters are

219 also estimated for each XKS waveform to verify azimuthal variation of the parameters. The
220 parameters of one-layer anisotropy for each station are presented here when the T-component
221 energy reduction is more than 30% and these parameters are in agreement with the mean values
222 of the individual splitting parameters. These parameters represent the anisotropic structure of a
223 dominant layer that affects the XKS waves for the observed azimuths.
224

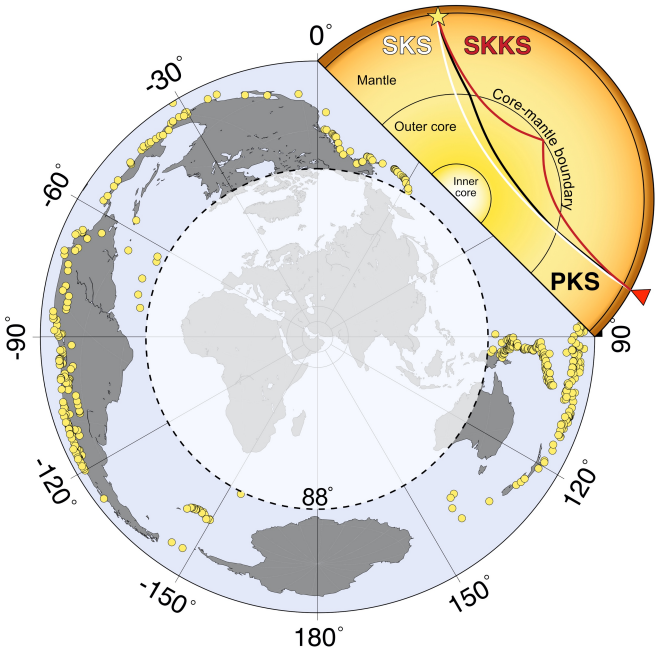

225

226 **Figure 3: Teleseismic earthquakes used to measure XKS splitting (yellow dots). Seismic phases used**
227 **in this study are illustrated in the top-right inset.**
228

229

230 **3. Results**

231 **3.1 Synthetic resolution tests of tomographic maps**

232 Solution robustness assessment is useful to assess the spatial resolution and sensitivity of
233 seismic features observed in tomographic models. Here, this is carried out through a series of
234 synthetic resolution experiments designed to test the trade-off between isotropic and anisotropic

variations in Rayleigh phase velocity. Resolution tests were initially performed separately for the isotropic and anisotropic components of the wavefield using a source-receiver configuration, as well as inversion parameters, identical to those for the observational dataset. The study area is parameterised through a grid node spacing of 0.1˚ in latitude and longitude. The starting velocity model is assumed to be isotropic and constant in the whole model space. This is implemented by associating the average phase velocity calculated for that particular period to each grid node, while the anisotropic coefficients are set to zero. The *a priori* data standard deviations and correlation lengths are set after analysis of the trade-off curves for each period (see Figure S4 for an example at 10 seconds). The *a priori* data standard deviation for the isotropic term was instead set to the phase-velocity uncertainty value determined for each individual measurement, which appears to correspond with the value obtained from the trade-off analysis (Figure S4). The noise is assumed to be uncorrelated, so the off-diagonal elements of the a priori data covariance matrix are zero and its diagonal elements are not all equal. An additional normally distributed error of 0.1 km/s was applied to each ray-path to simulate uncertainty associated with the observational dataset and adjust the amplitude of the model perturbations. Synthetic data are then inverted using the same tomographic inversion procedure described earlier with the goal of faithfully reconstructing two predetermined synthetic checkerboard inputs: one purely isotropic that is parameterised through an alternating pattern of higher and lower wave-speed variations (Figure 4), and the other only containing anisotropic variations with alternating blocks of NS and EW orientations, or different sets of fast-velocity orientations – one at N45 and another at N135 (Figure 5). Independently inverting both sets of synthetic traveltimes makes it possible to investigate whether anisotropy or isotropy is respectively introduced in the recovered models, when we previously assumed they are not required by the data. Additionally, we jointly invert

for isotropic and anisotropic terms (as done with the observational dataset), including synthetic structures that resemble those observed in our tomographic models. We include a 0.6 km/s variation from low to high velocity across the Semail thrust, and include a complex blocky variation of anisotropy orientations at 10 seconds (Figure 6).

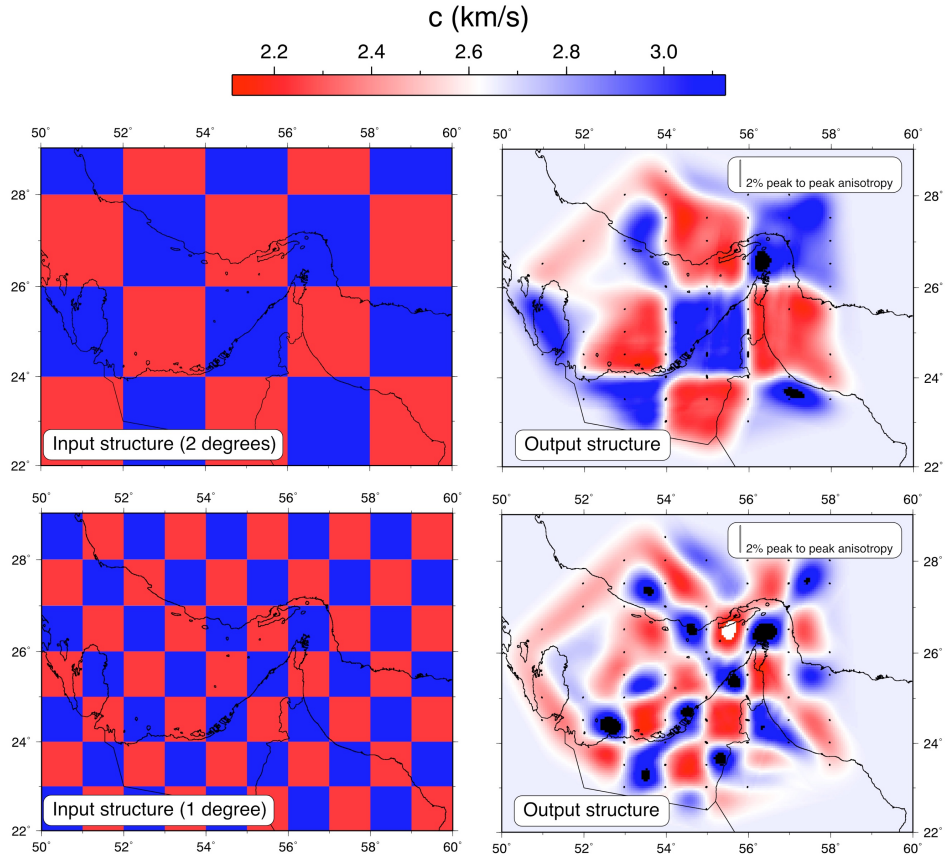

Figure 4: Comparison between input synthetic (1 and 2 degrees) and output models for isotropic velocities at 10 seconds. In the input checkerboard model, the anisotropy is set to zero. The output structures show little evidence of spurious anisotropy.

Figures 4 shows that the checkerboard velocity pattern is fairly well recovered through the isotropic inversion, particularly with structures as large as 2 degrees, although it does contain potentially misleading artefacts in peripheral regions. This is an expected effect due to the combination of lower ray-path coverage, deficiency of crossing paths information and a locally

dominant orientation of seismic raypaths, which have a tendency to smear out velocity anomalies in a specific direction. This is evident, for example, in the westernmost study area, where input structures are reproduced as elongated streaks and blurry anomalies. It can be noticed that the amount of spurious anisotropy introduced during the inversion is minimal throughout the model. Similarly, the recovery of the anisotropic NS and EW fast directions is good (Figure5), with the exception of western and eastern edge regions.

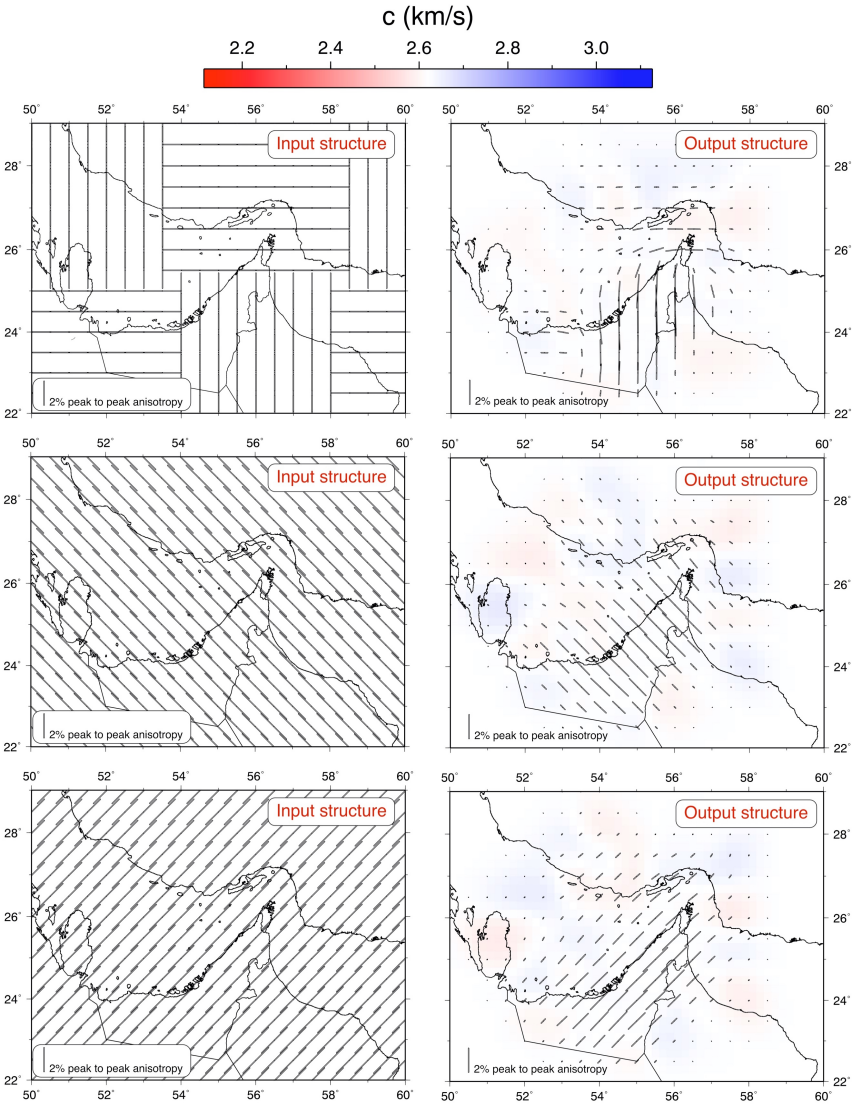

Figure 5: Comparison between input synthetic and output models for anisotropic terms at 10 seconds for the study area. In the input checkerboard model, the isotropy term is set to zero. The output structures show little evidence of spurious isotropy.

The retrieved models only see the appearance of relatively minor isotropic variations. A common feature in the isotropic and anisotropic input checkerboard patterns is that the interface between individual blocks exhibits a sharp discontinuity. Such dramatic changes are generally difficult to retrieve and result in a smooth transition through near zero anisotropy at the edge of each block (anisotropic model) or smooth velocity variation (isotropic model). This is, however, not surprising as it is an intrinsic property of regularised iterative non-linear schemes, hence a direct consequence of the inversion method used. Another common feature is that the pattern of anomalies is normally more reliable than their absolute amplitude. When anisotropy and isotropy are jointly inverted (Figure 6), resulting output structure show that the strong isotropic velocity discontinuity is well recovered, although it is not surprising that sharp anisotropic variations (i.e., 90˚) are slightly smoothed where strong discontinuities occur.

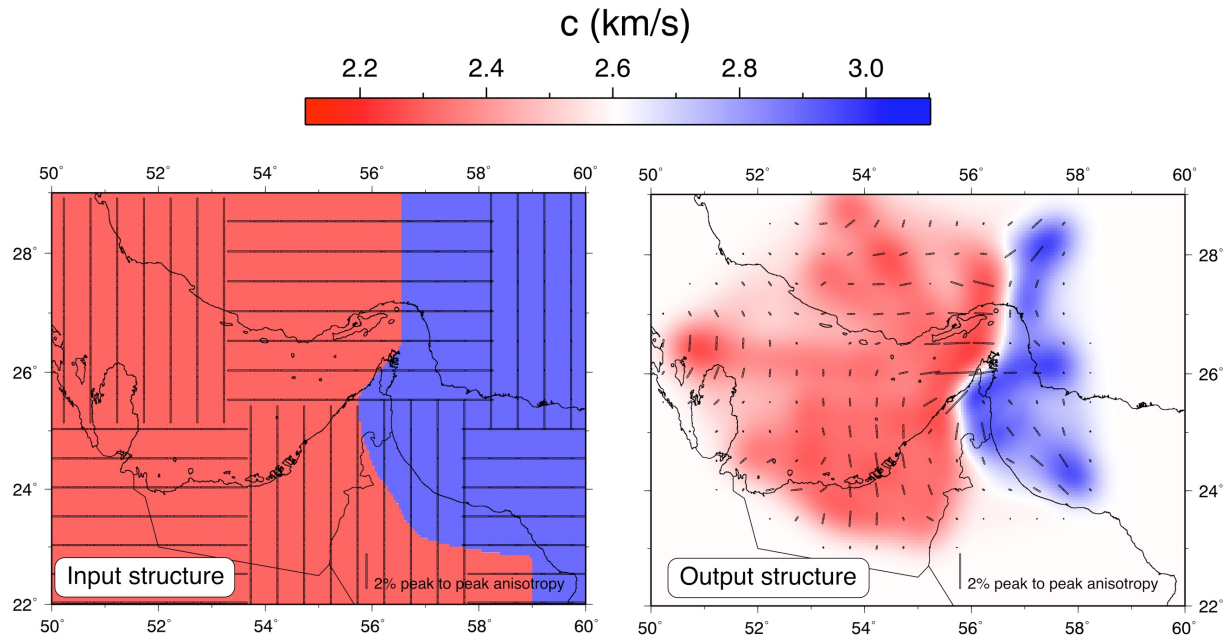

Figure 6: Synthetic test result from input synthetic structure involving a complex pattern of anisotropic terms and a strong, sharp velocity discontinuity. Isotropic and anisotropic terms are jointly inverted here (as per the observational dataset).

296 Overall, if a strong velocity change is present across the Semail thrust, this can be faithfully
297 recovered by our dataset and inversion method. Similarly, a 90˚ contrast of anisotropy
298 orientations in the northernmost Musandam peninsula can be recovered.
299
300
301 **3.2 Tomographic model**
302 Figure 7 shows the crustal structure beneath the northeastern Arabian plate margin via a
303 series of Rayleigh phase-velocity tomographic maps, onto which the orientation of the fast axes
304 of anisotropy have been superimposed. We present period-dependent maps at 5, 10, 15 and 25
305 seconds, which are broadly representative of the uppermost and lower crust (see sensitivity
306 kernels in Figure 7). The study area is parameterised using the same grid node spacing, a priori
307 model standard deviation and L_{corr} specified for the resolution tests (see section 3.1). The starting
308 velocity model is assumed to be isotropic and constant in the whole model space by assigning to
309 each grid node the average phase velocity determined for that particular period. The data
310 variance is on average reduced by 70% in the isotropic solution model.
311 The regional pattern of isotropic phase-velocity variations reveals the presence of a high
312 velocity area that spatially correlates with the surface expression of the UAE-Oman mountain
313 belt. This feature runs approximately landward of the eastern UAE and Oman shoreline and
314 appears to be flanked by low velocity anomalies. Indeed, phase velocities decrease by about 1
315 km/s where the Persian Gulf and the Gulf of Oman are known to be dominated by thick
316 sedimentary basins.
317

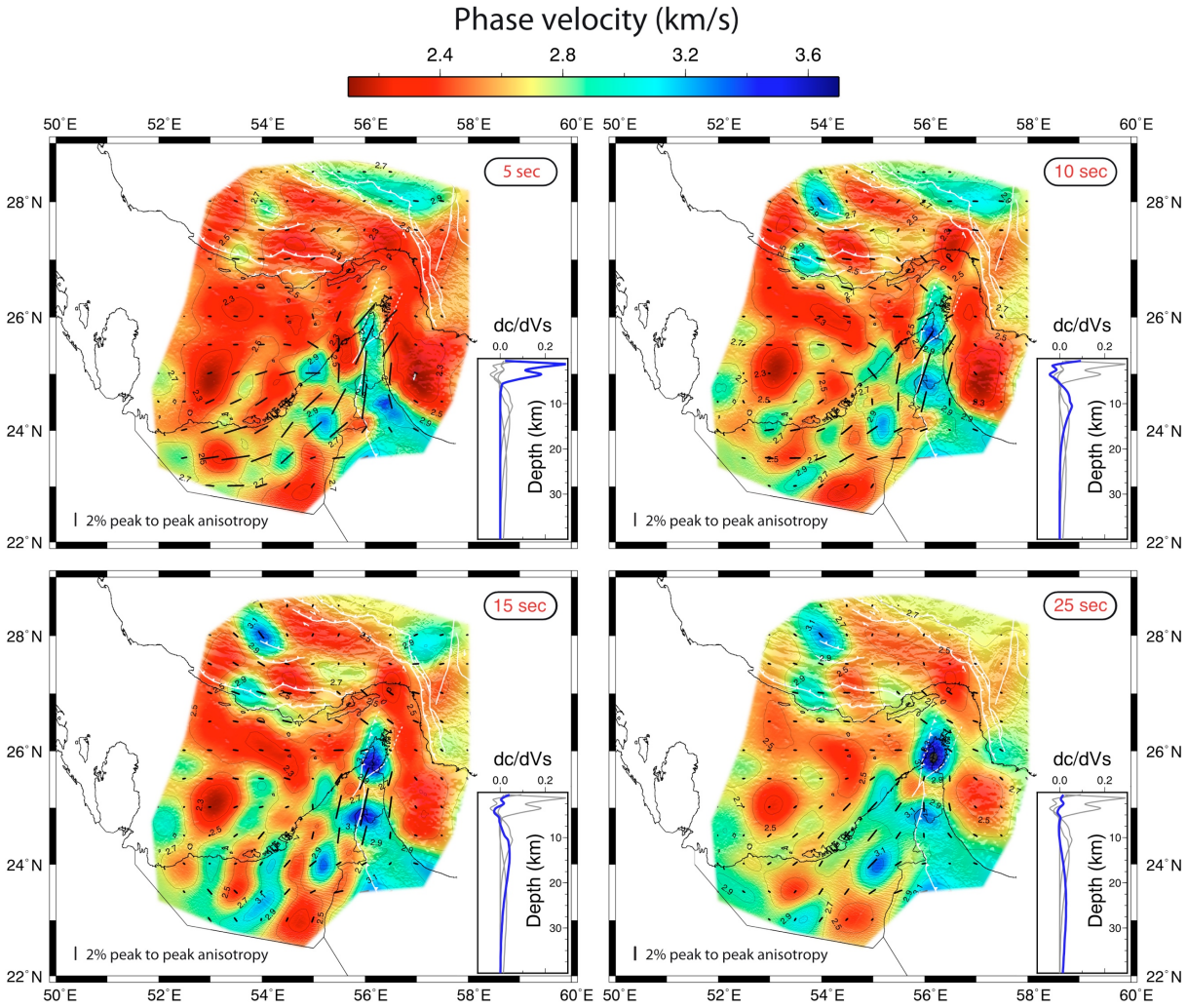

Figure 7: Final 2-D phase-velocity maps as a function of period illustrating both the isotropic (absolute variations of velocity) and anisotropic (black bars) components of the wave velocity field. Peak sensitivity of Rayleigh phase velocity occurs at a depth (in km) approximately equal to the period (in seconds), as shown by the sensitivity kernels (blue lines – grey lines are for comparison with other periods) in the bottom right inset of each map.

A prominent feature of the fast-azimuthal anisotropy directions is the sharp change occurring from the Musandam peninsula to the Zagros mountains (Figure 7). The fast directions are mostly trending nearly north-south in the UAE-Oman mountain belt to approximately WNW in the Strait of Hormuz and ZFTB. This divergence, however, should be viewed with caution since the more heterogeneous station coverage in Iran might be resulting in less robust

anisotropy strength and directions in the Zagros, as shown in Figure 5 and 6. Further to the southwest, fast anisotropy axes return to a dominantly northeast-southwest and east-west trend.

3.3 XKS measurements

As described in Section 2.2, we perform a joint analysis of XKS waveforms recorded at each station. When searching for the parameters of a one-layer model, the main assumption is that the XKS waves are mainly affected by anisotropy structure of a single layer within the range of the observed azimuths. To verify this assumption, we examined the azimuthal variation of the individual splitting parameters. A systematic azimuthal variation of splitting parameters for each station is taken as the first-order indication of depth-dependent anisotropy (Silver and Savage, 1994; Rümpker and Silver, 1998). However, as typical with temporary seismic networks, our limited azimuthal coverage does not allow for a full azimuthal coverage at most of the stations. Despite the limited azimuthal coverage, examination of the individual measurements indicates that the mean values of these measurements are in the agreement with parameters for the one-layer model obtained from the joint analysis. This examination suggests that the XKS are mainly affected by one layer of anisotropy within the observed azimuths.

The joint-analysis approach described in Section 2.2 allows to invert for two layers of anisotropy (azimuthal coverage permitting), albeit inverting for the splitting parameters for two-layer models is known to be a highly non-unique process (e.g., Latifi et al., 2018). As we are equipped with crustal anisotropy results from surface-wave tomography, we examine the effect of crustal anisotropy on the XKS splitting observation at a number of stations with adequate azimuthal coverage. At these locations, we search for two-layer models by fixing the fast direction of the upper layer in the direction of crustal anisotropy, as constrained by surface waves

(Figure S5). The theoretical curves of the two-layer models (Figure S5) show that crustal anisotropy could cause occurrence of apparently extreme values of XKS splitting parameters but at azimuths where we have only limited observations. Our two-layer modeling suggests that the effect of crustal anisotropy on our XKS analysis and one-layer inversion is negligible. Furthermore, the projection of individual splitting parameters onto two representative depths of 75 and 170 km (Figure S6 and S7) exhibits insignificant azimuthal variation of single measurements. This indicates that a one-layer model is a good approximation for the XKS observations at the majority of our stations.

Final results from our XKS analysis are shown in Figure 8, along with the splitting parameters in Table 1. Delay times across the region are on average 1.0 second, rather heterogeneously distributed and do not seem to follow an organized pattern. On the other hand, the dominant splitting orientation throughout the UAE-Oman mountains is remarkably consistent with an average orientation of 15˚ anticlockwise from the north, suggesting that in this location a single broad anisotropic feature is being resolved. Elsewhere, an approximately NE-SW orientation appears to dominate the pattern of anisotropy in the upper mantle.

4. Discussion

4.1 Seismic wavespeed and anisotropy in the crust

A consequence of the thrust-sheet load from the Semail ophiolite was the development of a peripheral bulge and flexure of the pre-existing underlying rift margin, with establishment of a foreland basin (Ali and Watts, 2009; Ali et al., 2020). Following the end of the obduction loading process, a so-called ‘hinterland’ (ten Brink & Stern, 1992) basin (up to 10 km thick) also

developed from subsidence in the Gulf of Oman. Tomographic maps in Figure 7 reveal a high-velocity body that spatially correlates to the UAE-Oman mountain belt, and is bounded by two low wave-speed anomalies, which we attribute to these flanking sedimentary basins. Similarly, sediments of the proto-Arabian passive margin in the Persian Gulf and the ZFTB dominate the tomographic images with slower wavespeeds. The eastern extent of the Semail ophiolite, marked in our tomographic maps as a strong lateral variation from high to low phase velocity, runs offshore in the vicinity of the coastline and concur with the location proposed by Ali et al. (2020) and Pilia et al. (2020b).

In the northern UAE-Oman orogenic belt, the fast azimuths of anisotropy appear to delineate a curved trend following the Dibba Fault and the Semail Thrust front, indicating parallelism between tectonic structure and anisotropy orientations. This implies that the seismic anisotropy we observe in the northern UAE-Oman belt, a region where Figures 5 and 6 demonstrate the model is well resolved, may be related to the tectonic fabric. However, we recognise that the direction of anisotropy is also similar to the strike of sheeted dikes (Nicolas et al., 2000) and the crystallographic preferred orientation of olivine found in the obducted Tethys upper mantle (Ambrose et al., 2018), although the Semail ophiolite is relatively thin in the onshore (Ali et al., 2020). Both stress-aligned shape-preferred orientation (SPO) and lattice preferred orientation (LPO) of the ophiolite aggregate minerals may therefore be contributing to the observed anisotropy. As the maximum horizontal stress directions inferred from the World Stress Map (Heidbach et al., 2016) show no parallelism with our anisotropy directions in the upper crust of the orogenic belt, we can potentially exclude the contribution of cracks in originating the observed anisotropy.

A striking feature of our tomographic results is the change in the fast-propagation traces from approximately WNW in the ZFTB and northern tip of the Musandam peninsula, to nearly NS in the UAE-Oman belt (Figures 7 and 9). In this region, the fast anisotropy axes support parallelism between tectonic fabric and anisotropy orientations. Orogen-parallel anisotropy observed in our tomographic model concurs with previous interpretations using seismic anisotropy at orogenic belts. For example, Fry et al. (2010) identified azimuthal anisotropy orientations to be normal to the direction of thrusting in the central Alps. Similarly, Pilia et al. (2016) and Bao et al. (2016) observed orogen-parallel anisotropy in the Tasmanides of Australia and the Cordillera (western Canada), respectively.

Since the western area of the UAE is obscured by a thick layer of Quaternary to recent sand dunes, it is impossible to infer any structural trend from the surface geological record. Comparison of the maximum horizontal stress directions, inferred from local borehole breakouts and drilling-induced tensile fractures (Noufal et al., 2016), with the anisotropy directions at 5 and 10 seconds yields an average difference of 20˚ in the onshore area and 70˚ in the offshore. We then exclude the hypothesis that cracks contribute to the observed anisotropy. While the Zagros collisional system is unlikely to have left an imprint in the tectonic fabric of the southwestern UAE crust, the pattern of anisotropy revealed here can potentially be explained by the structure inherited from extensional stresses (Kendall et al., 2006) that initiated faulting and rifting of the Arabian plate margin during the Mesozoic (i.e., anisotropy directions orthogonal to spreading direction). Indeed, normal faults in this region appear to have been reactivated as thrust faults during continental collision in the Zagros (Jackson, 1980). Therefore, it is not surprising that the strike of the structures detected in the Persian Gulf and southwest UAE resemble that of thrust faults found in the southern Zagros.

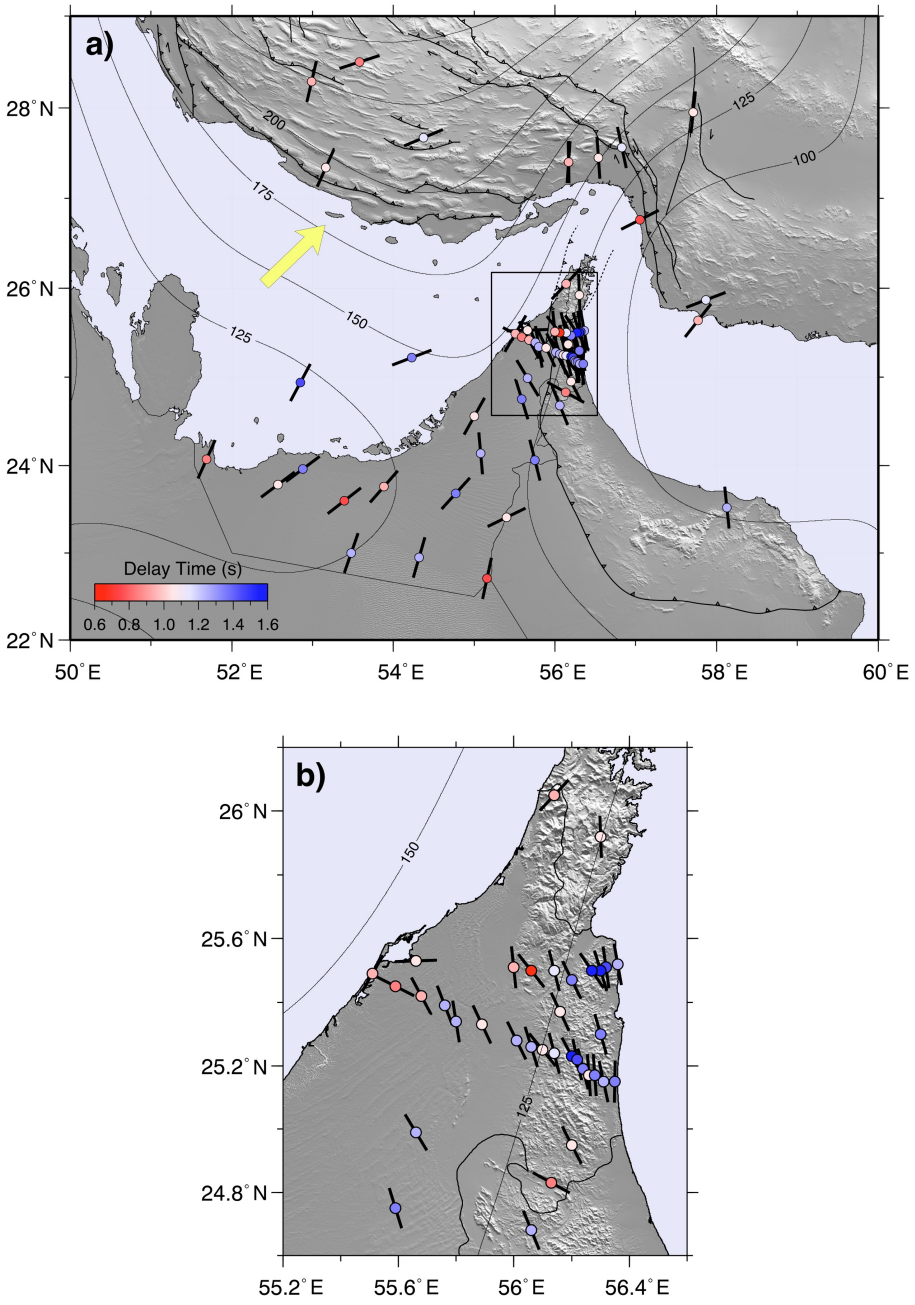

421

422 **Figure 8: Results from XKS analysis. a) XKS measurements at our stations with absolute plate**
423 **motion of 45.26 mm/yr (yellow arrow – ITRF reference frame), and lithospheric thickness contour**
424 **lines from Priestley and McKenzie (2013). b) Zoom-in on the two transects across the Musandam**
425 **Peninsula.**

426

427

428 **4.2 Mantle deformation beneath the Semail ophiolite**

By assuming that the lower mantle is not the main contributor to SKS splitting observations, we seek to explain our observations of mantle anisotropy in terms of lithospheric deformation and asthenospheric flow (Figures 8 and 9). Plate-driven viscous drag in the asthenosphere, for example, is typically advocated when fast-splitting orientations align with absolute plate motion. In the southwestern study area, which is underlain by the stable Precambrian Arabian basement, and beneath the ZFTB, the fast polarization orientations are consistent with the direction of Arabian plate motion (Figure 8). In contrast, seismic azimuthal anisotropy beneath the UAE-Oman mountain range is evidently diverging from the plate motion direction. Considering the relatively short length-scales variations in fast XKS polarization orientations (e.g., from 24.56˚N-55.0E to 25.64˚N-57.77˚E), which imply shallow sources of anisotropy (Alsina & Snieder, 1995), we seek to explain this pattern by invoking fossil anisotropy in the lithospheric mantle.

Previous surface wave tomographic studies identified a large contrast in lithospheric thickness, ranging from 90 km in the Gulf of Oman, to 250 km beneath the southcentral ZFTB (Priestley et al., 2012). This transition could potentially rework patterns of mantle flow through the generation of edge-driven convection (e.g., Ramsey & Pysklywec, 2011). In our results, such flow would be expected as either null-splitting where downwelling is predicted at the lithospheric discontinuity (or where there is a lack of lithospheric fabric), or at least as discontinuity-parallel splitting due to lateral flow. The latter is observed in the well-developed eastern Himalayan syntaxis, where both GPS velocities and mantle flow orientations wrap around the Namche Barwa syntaxis (Flesh et al., 2005), following indentation of the Indian plate. Since our observations suggest a dominant NW-SE oriented seismic anisotropy in this region

with little evidence for two layers of mantle anisotropy, we argue that the Strait of Hormuz syntaxis may disturb the asthenospheric flow but is not capable of modifying it.

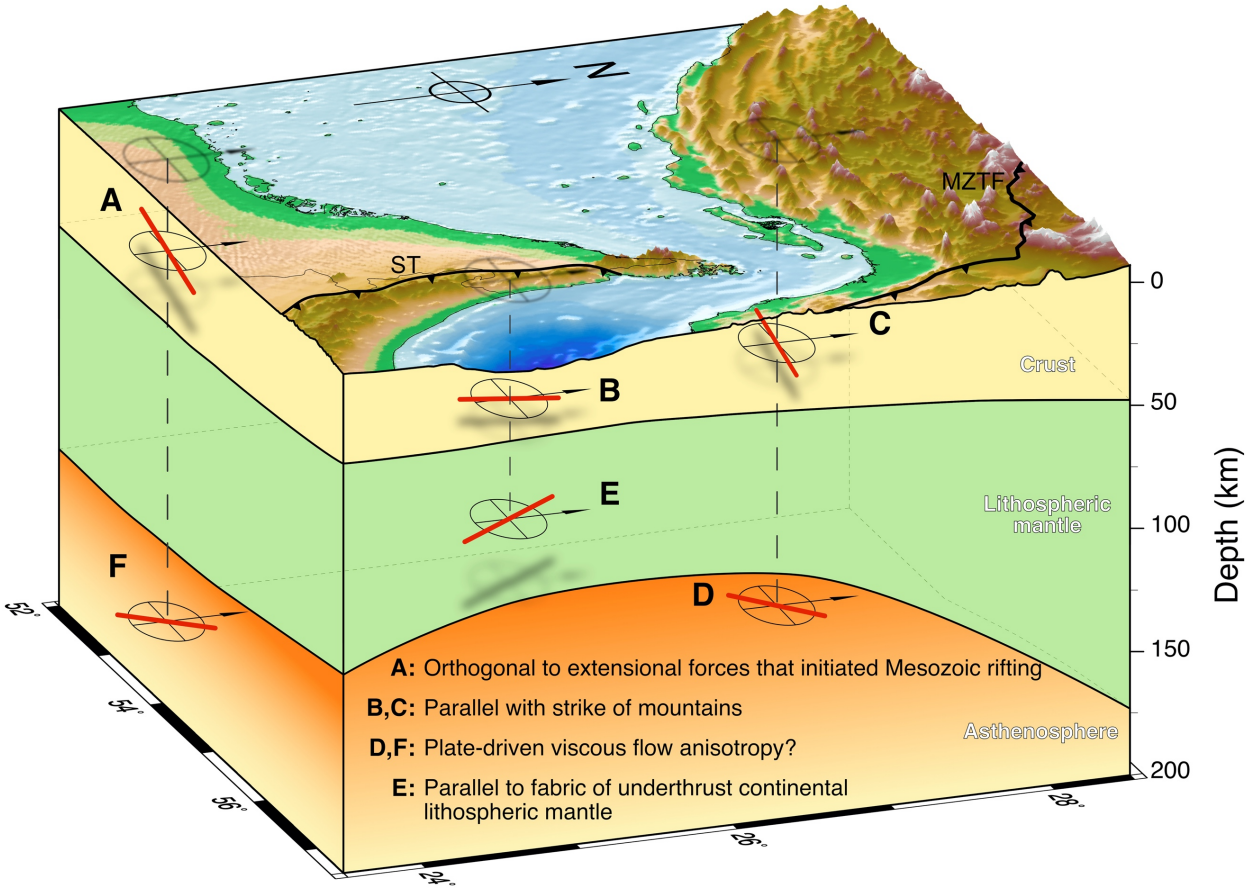

Figure 9: Conceptual illustration summarizing the anisotropy orientations observed in the lithosphere beneath the study area. Red bars are dominant orientations of anisotropy. Crustal and lithospheric thicknesses are consistent with Kaviani et al. (2020), and Priestley and McKenzie (2013), respectively.

While a number of stations in the eastern side of the seismic transects across the UAE-Oman mountain belt exhibit relatively high delay times, others do not. Additionally, when inspecting Figure 8, one can note that immediately to the north and south of the profiles there are a number of stations at similar longitude (e.g., II.UOSS, DN.HAT and OM.BAN) with fairly low delay times (about 1 second or lower delay times). These would not be expected if delay times

464 followed a hypothetical increasing trend from the foreland area to the mountains. Also, it is
465 unlikely that a lithospheric thickness variation of 25 km (which is about the vertical resolution of
466 the tomographic model of Priestley et al., 2012) can result in a delay-time variation of around 1
467 second. In Figure S8 the splitting parameters are plotted against longitude, and confirm that the
468 above-mentioned trend, if present, is very subtle.

469 Geological and geochronological data suggest that the Semail ophiolite formed above a
470 NE-dipping subduction zone 96-95 Ma (Rioux et al., 2016) and was emplaced from NE to SW
471 onto the rifted continental margin of Arabia from 95 – 79 Ma (Searle et al., 2003). In the UAE,
472 the lower crust appears to be tightly folded and thrust granulite-facies rocks formed at pressure–
473 temperature conditions of 11-15 kbar and 770-900ºC at 94.5 – 90 Ma (Searle et al., 2015b). In
474 the eastern part of the Oman mountains, meta-basic rocks intruded into Permian limestones along
475 the NE margin were transformed to eclogites at the deepest structural level (As Sifah eclogites)
476 indicating subduction of the leading edge of the continental margin to depths of ~80-90 km at
477 least in the eastern Oman mountains segment (Warren et al., 2003; Searle, 2007). Following
478 exhumation of the high-temperature granulites in the UAE and high-pressure eclogites at As
479 Sifah in Oman, the whole obduction process ended by ~68 Ma with Upper Maastrichtian clastic
480 sediments unconformably overlying all units. This is the last significant deformational episode
481 recorded in the northern Musandam peninsula. A return to stable, shallow marine conditions
482 from Upper Maastrichtian to Eocene time was followed by post-Eocene gentle folding of the
483 entire mountains. We argue that the persistent fast-polarization orientations localized in the
484 UAE-Oman mountains region derive from the frozen-in deformation inherited from the
485 continental lithospheric mantle during underthrusting of the Arabian passive margin (Figure 9).
486

5 Conclusions

A new seismic network in the UAE has allowed us to constrain crustal and mantle deformation using anisotropic tomography and shear-wave splitting analysis. The compelling degree of consistency between the orientation of fast anisotropy axes and tectonic fabric seen in the crust, marking a rotation of ~90˚ from the southern Zagros to the UAE-Oman belt, is a record of diachronous deformation associated with transition from Late Cretaceous ophiolite obduction to Eocene early continental collision. It is likely that the two orthogonal anisotropy orientations revealed by our model stem from the orogenic processes relative to obduction of the Semail ophiolite and continental collision in the Zagros mountains. Consistency between fast-polarization orientations localized in the UAE-Oman belt and the strike of the Oman subduction zone suggests that the anisotropy signature in the lithospheric mantle has retained a pattern that dates back to the time of Late Cretaceous obduction of the Semail ophiolite (Figure 9). Our data corroborates previous geological evidence on the geometry of the NE-dip of the Oman subduction system, the orthogonal emplacement of thrust sheets, and provides the first direct geophysical evidence from the mantle lithosphere.

Acknowledgments

S.P. acknowledges support from the Natural Environmental Research Council (NERC) Grant NE/R013500/1 and from the European Union's Horizon 2020 research and innovation program under Marie Skłodowska-Curie Grant Agreement 790203. Data acquisition in the UAE was partially supported by The Petroleum Institute Research Centre Project LTR14011. We thank Brook Keats and Tyler Ambrose for insightful discussions about the tectonics of the Semail ophiolite. We are grateful to the Iranian Seismological Center and NCM for providing

daily noise records from broadband stations in Iran and the remaining stations used in this study, respectively. The dataset used in this study is from Pilia et al. (2020a).

514

515 **Table 1: Splitting parameters for stations shown in Figure 8.**

Station	Sta_Lat	Sta_Lon	Phi	dt
AE.AJN	24.56	55.00	29	1.0
AE.ALN	24.06	55.75	-14	1.3
AE.JRN	24.94	52.85	28	1.4
AE.MSF	25.37	56.16	-25	1.0
AE.MZR	23.00	53.48	19	1.2
AE.SHM	26.05	56.14	43	0.9
AE.SRB	25.22	54.23	69	1.3
AE.UMQ	25.53	55.66	88	1.0
BI.BNDS	27.40	56.17	-1	0.9
BI.CHBR	25.60	60.48	4	0.8
BI.GHIR	28.29	52.99	13	0.9
DN.FAQ	24.75	55.59	-17	1.3
DN.HAT	24.83	56.13	-61	0.8
DN.NAZ	24.99	55.66	-31	1.2
II.UOSS	24.95	56.20	-27	1.0
IR.BNB	27.45	56.54	-4	1.0
IR.GENO	27.40	56.17	4	0.9
IR.JASK	25.87	57.87	69	1.1
IR.JHRM	28.50	53.58	72	0.8
IR.JSK1	25.64	57.77	38	0.9
IR.KHNJ	27.95	57.71	6	1.0
IR.KHSK	26.76	57.05	63	0.7
IR.LAR1	27.67	54.37	67	1.1
IR.LMD1	27.34	53.16	24	1.0
IR.NGCH	25.36	61.14	26	1.1
IR.NIAN	27.56	56.83	-12	1.1
IR.SRVN	27.40	62.40	-43	1.1
OM.ASH	24.68	56.06	-22	1.2
OM.BAN	25.92	56.30	-2	1.0
OM.BID	23.52	58.13	-6	1.2
OM.MDH	25.30	56.30	-16	1.3
OM.SOH	24.13	56.53	19	1.1
UE.GHWR	23.96	52.88	53	1.3
UE.MZWR	23.76	53.88	41	0.9
UE.SLWR	24.07	51.69	24	0.8
UE.UMZA	22.71	55.16	12	0.7
XX.STN01	25.49	55.51	30	0.9
XX.STN02	25.45	55.59	-63	0.8
XX.STN03	25.42	55.68	-28	0.9
XX.STN04	25.39	55.76	-21	1.2
XX.STN05	25.34	55.80	-9	1.2
XX.STN06	25.33	55.89	-25	1.0

XX.STN07	25.28	56.01	-26	1.2
XX.STN08	25.26	56.06	-17	1.2
XX.STN09	25.25	56.10	-39	1.0
XX.STN10	25.24	56.14	-14	1.1
XX.STN11	25.23	56.20	-28	1.5
XX.STN12	25.22	56.22	-12	1.4
XX.STN13	25.19	56.24	-14	1.3
XX.STN14	25.17	56.26	-4	1.0
XX.STN15	25.17	56.28	-4	1.3
XX.STN16	25.15	56.31	-12	1.2
XX.STN17	25.15	56.35	1	1.3
XX.STN18	25.52	56.36	-10	1.2
XX.STN19	25.51	56.32	-8	1.4
XX.STN20	25.50	56.30	-17	1.5
XX.STN21	25.50	56.27	-34	1.5
XX.STN22	25.47	56.20	-26	1.3
XX.STN23	25.50	56.14	-14	1.1
XX.STN24	25.50	56.06	-38	0.6
XX.STN25	25.51	56.00	-6	0.9
XX.STN27	24.14	55.08	-5	1.2
XX.STN28	23.68	54.77	42	1.3
XX.STN29	23.41	55.40	64	1.0
XX.STN30	22.95	54.32	16	1.2
XX.STN31	23.60	53.39	52	0.7
XX.STN32	23.78	52.57	53	1.0

516

517

518

519

Rreferences

Ali, M.Y. and Watts, A.B., 2009, Subsidence history, gravity anomalies and flexure of the United Arab Emirates (UAE) foreland basin. GeoArabia, 14(2), p.17-44.

Ali, M.Y., Aidarbayev, S., Searle, M.P. and Watts, A.B., 2017, Subsidence history and seismic stratigraphy of the western Musandam peninsula, Oman – United Arab Emirates Mountains. Tectonics, 37, doi: 10.1002/2017TC004777.

Ali, M.Y., Watts, A.B., Searle, M.P., Keats, B., Pilia, S. and Ambrose, T., 2020, Geophysical imaging of ophiolite structure in the United Arab Emirates. Nature Communications, 11(1), pp.1-10, doi: 10.1038/s41467-020-16521-0.

Alsina, D. and Snieder, R., 1995, Small-scale sublithospheric continental mantle deformation: constraints from SKS splitting observations. Geophysical Journal International, 123(2), pp.431-448, doi: 10.1111/j.1365-246X.1995.tb06864.x.

Ambrose, T. K., Wallis, D., Hansen, L. N., Waters, D. J., & Searle, M. P., 2018, Controls on the rheological properties of peridotite at a palaeosubduction interface: A transect across the base of the Oman-UAE ophiolite. Earth and Planetary Science Letters, 491, 193 - 206. doi: https://doi.org/10.1016/447_j.epsl.2018.03.027

Babuska, V., and M. Cara, 1991, Seismic Anisotropy in the Earth, vol. 10, Springer, Netherlands.

Bao, X., Eaton, D.W. and Gu, Y.J., 2016, Rayleigh wave azimuthally anisotropic phase velocity maps beneath western Canada. Journal of Geophysical Research: Solid Earth, 121(3), p.1821-1834, doi: 10.1002/2015JB012453.

Bowman, J. R., and Ando, M., 1987, Shear-wave splitting in the upper-mantle wedge above the Tonga subduction zone, Geophys. J. R. Astron. Soc., 88, 25– 41. doi:10.1111/j.1365-246X.1987.tb01367.x.

Crampin, S. 1994, The fracture criticality of crustal rocks, Geophysical Journal International, 118(2), 428–438, doi:10.1111/j.1365-246X.1994.tb03974.x.

Debayle, E. and Sambridge, M., 2004, Inversion of massive surface wave data sets: Model construction and resolution assessment. Journal of Geophysical Research: Solid Earth, 109(B2), doi: 10.1029/2003JB002652.

Flesch, L.M., Holt, W.E., Silver, P.G., Stephenson, M., Wang, C.Y. and Chan, W.W., 2005, Constraining the extent of crust–mantle coupling in central Asia using GPS, geologic,

and shear wave splitting data. Earth and Planetary Science Letters, 238(1-2), pp.248-268, https://doi.org/10.1016/j.epsl.2005.06.023.

Fry, B., Deschamps, F., Kissling, E., Stehly, L. and Giardini, D., 2010, Layered azimuthal anisotropy of Rayleigh wave phase velocities in the European Alpine lithosphere inferred from ambient noise. Earth and Planetary Science Letters, 297(1-2), p. 95-102, https://doi.org/10.1016/j.epsl.2010.06.008.

Glennie, K., Boeuf, M., Clarke, M. H., Moody-Stuart, M., Pilaar, W., and Reinhardt, B., 1973, Late Cretaceous nappes in Oman Mountains and their geologic evolution. AAPG Bulletin, 57 (1), p. 5-27.

Heidbach, O., Rajabi, M., Reiter, K., Ziegler, M., & Wsm Team. (2016). World stress map database release 2016. GFZ Data Services.

Jackson, J. 1980, Reactivation of basement faults and crustal shortening in orogenic belts. Nature, 283 (5745), 343, doi: https://doi.org/10.1038/283343a0.

Kaviani, A., Paul, A., Moradi, A., Mai, P.M., Pilia, S., Boschi, L., Rümpker, G., Lu, Y., Tang, Z. and Sandvol, E., 2020, Crustal and uppermost mantle shear-wave velocity structure beneath the Middle East from surface-wave tomography. Geophysical Journal International. https://doi.org/10.1093/gji/ggaa075.

Kendall, J.M., Pilidou, S., Keir, D., Bastow, I.D., Stuart, G.W. and Ayele, A., 2006, Mantle upwellings, melt migration and the rifting of Africa: Insights from seismic anisotropy. Geological Society, London, Special Publications, 259(1), p.55-72, doi: 10.1144/GSL.SP.2006.259.01.06.

Latifi, K., Kaviani, A., Rümpker, G., Mahmoodabadi, M., Ghassemi, M.R. and Sadidkhouy, A., 2018, The effect of crustal anisotropy on SKS splitting analysis—synthetic models and real-data observations. Geophysical Journal International, 213(2), p.1426-1447, doi: 10.1093/gji/ggy053

Menke, W., and V. Levin, 2003, A cross-convolution method for interpreting SKS splitting observations, with application to one and two layer anisotropic earth models, Geophys. J. Int., 154, p. 379– 392, doi: 10.1046/j.1365-246X.2003.01937.x.

Montagner, J., 1986, Regional three-dimensional structures using long-period surface waves. Ann. Geophys , 4 (B3), 283-294.

Montagner, J.-P., & Nataf, H.-C., 1986, A simple method for inverting the azimuthal anisotropy

of surface waves. Journal of Geophysical Research: Solid Earth, 91 (B1), 511-520, doi: 10.1029/JB091iB01p00511

Morris, A., Meyer, M., Anderson, M.W. and MacLeod, C.J. 2016, Clockwise rotation of the entire Oman ophiolite occurred in a suprasubduction zone setting. Geology, 44(12), 1055-1058, doi: 10.1130/G38380.1

Nicolas, A., Boudier, F., Ildefonse, B., & Ball, E. 2000, Accretion of Oman and United Arab Emirates ophiolite - Discussion of a new structural map. Marine Geophysical Researches, 21 (3), 147-180. doi: 10.1023/A:1026769727917

Noufal, A., Obaid, K., & Ali, M., 2016, Abu Dhabi Stress Map. ADIPEC, Abu Dhabi. SPE-182919 .

Paul, A., Kaviani, A., Hatzfeld, D., Vergne, J. and Mokhtari, M., 2006, Seismological evidence for crustal-scale thrusting in the Zagros mountain belt (Iran). Geophysical Journal International, 166(1), pp.227-237, https://doi.org/10.1111/j.1365-246X.2006.02920.x.

Pilia, S., Arroucau, P., Rawlinson, N., Reading, A. M., and Cayley, R. A., 2016, Inherited crustal deformation along the East Gondwana margin revealed by seismic anisotropy tomography. Geophysical Research Letters, v. 43(23), p. 12-082, https://doi.org/10.1002/2016GL071201.

Pilia, S., Jackson, J. A., Hawkins, R., Kaviani, A., and Ali, M. Y., 2020a, The southern Zagros collisional orogen: new insights from transdimensional-trees inversion of seismic noise. Geophysical Research Letters, https://doi.org/10.1029/2019GL086258.

Pilia, S., Hu, H., Ali, M. Y., Rawlinson, N., & Ruan, A. 2020b, Upper mantle structure of the northeastern Arabian Platform from teleseismic body-wave tomography. Physics of the Earth and Planetary Interiors, 307, 106549. https://doi.org/10.1016/j.pepi.2020.106549

Priestley, K., McKenzie, D., Barron, J., Tatar, M. and Debayle, E., 2012, The Zagros core: deformation of the continental lithospheric mantle. Geochemistry, Geophysics, Geosystems, 13(11), https://doi.org/10.1029/2012GC004435.

Priestley, K. and McKenzie, D., 2013, The relationship between shear wave velocity, temperature, attenuation and viscosity in the shallow part of the mantle. Earth and Planetary Science Letters, 381, p.78-91, https://doi.org/10.1016/j.epsl.2013.08.022.

Ramsay, T. and Pysklywec, R., 2011, Anomalous bathymetry, 3D edge driven convection, and dynamic topography at the western Atlantic passive margin. Journal of

613 Geodynamics, 52(1), p.45-56, https://doi.org/10.1016/j.jog.2010.11.008
614 Rawlinson, N., Arroucau, P., Musgrave, R., Cayley, R., Young, M. and Salmon, M., 2014,
615 Complex continental growth along the proto-Pacific margin of East Gondwana.
616 Geology, 42(9), p.783-786, doi: 10.1130/G35766.1
617 Reiss, M.C., and Rümpker; G., 2017, SplitRacer: MATLAB Code and GUI for Semiautomated
618 Analysis and Interpretation of Teleseismic Shear-Wave Splitting, Seismological Research
619 Letters, 88 (2A): 392–409. doi: 10.1785/0220160191.
620 Rioux, M., Garber, J., Bauer, A., Bowring, S., Searle, M., Kelemen, P., and Hacker, B., 2016,
621 Synchronous formation of the metamorphic sole and igneous crust of the Semail
622 ophiolite: New constraints on the tectonic evolution during ophiolite formation from
623 high-precision U-Pb zircon. Earth and Planetary Science Letters, 451, pp.185-195,
624 https://doi.org/10.1016/j.epsl.2016.06.051.
625 Rümpker, G., & Silver, P. G. (1998). Apparent shear-wave splitting parameters in the presence
626 of vertically varying anisotropy. *Geophysical Journal International,* 135(3), 790-800.
627 https://doi.org/10.1046/j.1365-246X.1998.00660.x
628 Schimmel, M., Stutzmann, E., & Gallart, J. 2011, Using instantaneous phase coherence for signal
629 extraction from ambient noise data at a local to a global scale. Geophysical Journal
630 International, 184(1), 494–506. doi: 10.1111/j.1365-246X.2010.04861.x
631 Searle, M. P., 1988, Structure of the Musandam culmination (Sultanate of Oman and United
632 Arab Emirates) and the Straits of Hormuz syntaxis. Journal of the Geological
633 Society, 145(5), p. 831-845, https://doi.org/10.1144/gsjgs.145.5.0831.
634 Searle, M.P., Warren, C.J., Waters, D.J. and Parrish, R.R., 2003, Subduction zone polarity in the
635 Oman Mountains: implications for ophiolite emplacement. Geological Society, London,
636 Special Publications, 218(1), p.467-480, https://doi.org/10.1144/GSL.SP.2003.218.01.24.
637 Searle, M.P., 2007, Structural geometry, style and timing of deformation in the Hawasina
638 Window, Al Jabal al Akhdar and Saih Hatat culminations, Oman
639 Mountains. GeoArabia, 12(2), pp.99-130.
640 Searle, M.P., Cherry, A.G., Ali, M.Y. and Cooper, D.J., 2014, Tectonics of the Musandam
641 Peninsula and northern Oman Mountains: From ophiolite obduction to continental
642 collision. GeoArabia, 19(2), pp.135-174.
643 Searle, M.P. 2015a, Mountain Building, Tectonic evolution, Rheology, and Crustal Flow in the

644 Himalaya, Karakoram, and Tibet. In: Schubert, G. (Ed) Treatise of Geophysics, vol. 6,
645 469-511, http://dx.doi.org/10.1016/B978-0-444-53802-4.00121-4.
646 Searle, M.P., Waters, D.J., Garber, J.M., Rioux, M., Cherry, A.G. and Ambrose, T.K. 2015b.
647 Structure and metamorphism beneath the obducting Oman ophiolite: Evidence from the
648 Bani Hamid granulites, northern Oman mountains. Geosphere, 11(6),
649 doi:10.1130/GES01199.1
650 Searle, M., 2019. Geology of the Oman Mountains, Eastern Arabia. Springer, 478p.
651 Silver, P. G., & Savage, M. K. (1994). The interpretation of shear-wave splitting parameters in
652 the presence of two anisotropic layers. *Geophysical Journal International,* 119(3), 949-
653 963. https://doi.org/10.1111/j.1365-246X.1994.tb04027.x
654 Smith, M. L., and Dahlen, F., 1973, The azimuthal dependence of Love and Rayleigh wave
655 propagation in a slightly anisotropic medium. Journal of Geophysical Research, 78 (17),
656 3321-3333, doi: 10.1029/JB078i017p03321
657 ten Brink, U., & Stern, T. 1992, Rift flank uplifts and hinterland basins: comparison of the
658 Transantarctic Mountains with the Great Escarpment of southern Africa. *Journal of*
659 *Geophysical Research: Solid Earth,* 97(B1), 569-585. https://doi.org/10.1029/91JB02231
660 Tilton, G.R., Hopson, C.A. and Wright, J.E., 1981, Uranium-lead isotopic ages of the Samail
661 ophiolite, Oman, with applications to Tethyan ocean ridge tectonics. Journal of
662 Geophysical Research: Solid Earth, 86(B4), p. 2763-2775,
663 https://doi.org/10.1029/JB086iB04p02763.
664 Ventosa, S., Schimmel, M., & Stutzmann, E., 2017, Extracting surface waves, hum and normal
665 modes: Time-scale phase-weighted stack and beyond. Geophysical Journal International,
666 211(1), 30–44. Doi: 10.1093/gji/ggx284
667 Warren, C.J., Parrish, R.R., Searle, M.P. and Waters, D.J., 2003, Dating the subduction of the
668 Arabian continental margin beneath the Semail ophiolite, Oman. Geology, 31(10), p.889-
669 892, https://doi.org/10.1130/G19666.1.
670 Yao, H., van Der Hilst, R.D. and De Hoop, M.V., 2006, Surface-wave array tomography in SE
671 Tibet from ambient seismic noise and two-station analysis - I. Phase velocity
672 maps. Geophysical Journal International, 166(2), pp.732-744, doi: 10.1111/j.1365-
673 246X.2006.03028.x.

674